Variational Transition State Theory Study on the Alcohol Formation Reactions of Formaldehyde Oxide with Methane and Ethane

Kuan-Yi Chou , Yi-Wen Chen , Yu-Ting Wang , Wei-Ping Hu *

Posted Date: 28 November 2025

doi: 10.20944/preprints202511.2205.v1

Keywords: Criegee intermediates; variational transition state theory; multi-dimensional tunneling; dual-level dynamics; kinetic isotope effects; heavy atom tunneling

 doi:10.20944/preprints202511.2205.v1

Article

Variational Transition State Theory Study on the Alcohol Formation Reactions of Formaldehyde Oxide with Methane and Ethane

Kuan-Yi Chou, Yi-Wen Chen, Yu-Ting Wang and Wei-Ping Hu *

Department of Chemistry and Biochemistry, National Chung Cheng University, Chia-Yi, Taiwan 62102
* Correspondence: chewph@ccu.edu.tw

Abstract

The reactions of formaldehyde oxide (CH_2OO) with methane and ethane that yield alcohol products were investigated using dual-level variational transition state theory with multidimensional tunneling corrections (VTST/MT). Additional systems—including halogenated formaldehyde oxides (CF_2OO and CCl_2OO), deuterated alkanes (CD_4, C_2D_6), and isotopically substituted formaldehyde oxide ($CH_2{}^{18}O{}^{18}O$)—were also examined to explore substituent and isotope effects. Bimolecular rate constants and kinetic isotope effects (KIEs) were computed over the temperature range of 100–600 K. Significant tunneling contributions were predicted, especially below room temperature, where tunneling increases the rate constants of the CH_2OO + alkane reactions by up to two orders of magnitude. The computed H/D KIEs are approximately 3 at 300 K and rise to ~10 at 200 K. Notably, pronounced oxygen tunneling was also observed, giving ^{18}O KIEs of ~1.2 at 300 K and ~2.2 at 200 K. Halogen substitution was predicted to substantially reduce reaction barriers due to the weakening of the O–O bond, leading to rate constants for CF_2OO reactions that exceed those of CH_2OO by more than ten orders of magnitude at 300 K. The mechanisms underlying the strong tunneling effects, the individual contributions to the calculated KIEs, and the implications of these findings for atmospheric chemistry are discussed.

Keywords: Criegee intermediates; variational transition state theory; multi-dimensional tunneling; dual-level dynamics; kinetic isotope effects; heavy atom tunneling

1. Introduction

Criegee intermediates (CIs) are highly reactive zwitterionic species[1] that play a crucial role in atmospheric chemistry. These intermediates are primarily formed during the ozonolysis of alkenes[2] and contribute significantly to atmospheric oxidation processes, including reactions with volatile organic compounds (VOCs), nitrogen oxides (NO_x), and sulfur dioxide (SO_2).[3–5] Their high reactivity makes them key participants in secondary organic aerosol (SOA) formation[6,7] and radical chemistry.[8–10] In addition, CIs have attracted interest in synthetic chemistry because they can promote oxidation reactions under relatively mild conditions. While the reactivity of Criegee intermediates has been extensively investigated with common atmospheric molecules such as water and carbonyl compounds,[11–14] the chemistry of halogenated CIs has received comparatively less attention.

Halogenated CIs may be generated from the ozonolysis of halogenated alkenes of anthropogenic origin,[15] such as those emitted from industrial activities in the petrochemical, semiconductor, and refrigerant sectors.[16] In these industries, chlorinated and fluorinated alkenes (haloalkenes) such as chloroethylene (CH_2=CHCl), tetrachloroethylene (CCl_2=CCl_2), fluoroethylene (CH_2=CHF),

 doi:10.20944/preprints202511.2205.v1

tetrafluoroethylene (CF_2=CF_2), and hydrofluoroolefins (HFOs; e.g., HFO-1234yf and HFO-1234ze) are widely used as monomers, solvents, or working fluids.[17–23] Their ozonolysis can generate a variety of halogenated Criegee intermediates—including CHClOO, CCl_2OO, CHFOO, CF_2OO, and CF_3CHOO—that exhibit distinct electronic effects and substitution patterns. These structural features can markedly influence their reactivity toward atmospheric oxidants and thereby contribute to secondary pollution processes such as oxidant formation and aerosol generation.[24,25] Investigating halogenated CIs is thus essential for understanding the chemical impacts of industrial emissions and for assessing their broader environmental risks.[26–32] Recent laboratory advances in producing and detecting Criegee intermediates[33–36] have made it possible to examine reactions of simple CIs with atmospheric molecules, motivating further theoretical investigations.

Alkanes, including methane, ethane, and higher hydrocarbons, are major components of natural gas and anthropogenic emissions.[37–42] Among them, methane and ethane are of particular concern owing to their high global warming potential.[43] Reactions of CIs with methane and ethane offer possible atmospheric oxidation pathways that may affect the lifetimes of these alkanes as well as the formation of secondary oxidation products. Elucidating these reactions at the molecular level is therefore important for a more complete understanding of atmospheric oxidation chemistry. Furthermore, reactions between CIs and alkanes may contribute to the formation of alcohols in the atmosphere.

Beyond their atmospheric relevance, such CI alkane reactions also suggest a potential green-chemistry route for producing methanol and ethanol—key platform chemicals used as fuels, industrial solvents, and feed–stocks for chemical synthesis. Conventional industrial methods for methanol production, such as syngas conversion,[44] typically require high temperatures and pressures, resulting in substantial energy consumption and associated carbon emissions. Similarly, ethanol is mainly produced via fermentation[45] or ethylene hydration,[46] both of which present environmental and energy-related limitations. CI-mediated oxidation of alkanes may thus offer an alternative pathway to alcohols under near-ambient conditions, potentially reducing both the carbon footprint and reliance on traditional fossil-based processes.

The reactions between the simplest CI, formaldehyde oxide (CH_2OO), and simple alkanes have been investigated by Xu *et al*.[47] using electronic structure calculations combined with conventional transition state theory (TST). Their results revealed substantial barrier reductions for reactions involving halogenated CIs. However, for reactions that involve significant hydrogen motion along the reaction coordinate, tunneling effects must be taken into account,[48,49] especially when the reaction barriers are appreciable. Moreover, the alcohol-forming reactions considered here also involve transfer (or insertion) of oxygen atoms, so oxygen tunneling[50] may further enhance the reaction rate constants at lower temperatures.

In the present study, we apply dual-level variational transition state theory[51–53] with multidimensional tunneling[54–56] (VTST/MT) to investigate the rate constants of the alcohol-forming reactions of formaldehyde oxide and halogenated formaldehyde oxides (CF_2OO and CCl_2OO) with methane and ethane over the temperature range of 100–600 K. Kinetic isotope effects (KIEs) are powerful probes of reaction mechanisms and tunneling contributions.[57,58] Accordingly, we calculate and analyze both deuterium KIEs, using deuterated alkanes, and ^{18}O KIEs arising from isotopically substituted formaldehyde oxide.

2. Computational Details

Geometry optimizations and harmonic vibrational frequency calculations for all reactants, products, and transition states were carried out using the MP2[59] theory with the aug-cc-pVDZ basis set.[60,61] Single-point energies at these stationary points were computed using CCSD(T)/aug-cc-pVnZ (n = T, Q), followed by extrapolation to the complete basis set (CBS) limit. [62–65] The CBS-extrapolated energies (by the two-point extrapolation formula of Helgaker *et al*.[62]) were used as the "high-level" energetic reference. The minimum-energy paths (MEPs), including geometries, energies,

 doi:10.20944/preprints202511.2205.v1

gradients, and Hessians, were calculated at the MP2/aug-cc-pVDZ level, which served as the "low-level" potential energy surface (PES). Step sizes of 0.002 and 0.010 bohr were used for gradient and Hessian stepping, respectively, in mass-scaled coordinates using the Page–McIver algorithm[66,67] with a scaling mass of 1 amu. Cartesian coordinates and the harmonic approximation were used to compute vibrational frequencies and zero-point energies of the generalized transition states along each MEP.

To balance accuracy and efficiency, bimolecular rate constants were calculated using a dual-level variational transition state theory approach based on the Seckart interpolation scheme.[68–70] In this method, molecular geometry, vibrational properties, and reaction-path curvature are obtained from the low-level PES, while the energetics along the reaction path are corrected using the high-level energies at the reactants, transition states, and products. Energy values between stationary points are interpolated using the differences between low- and high-level data to produce a smooth corrected PES. This protocol preserves the reliable low-level description of the reaction coordinate while incorporating high-accuracy barrier heights and reaction energies, which is especially important when tunneling plays a major role.

Canonical variational transition state theory (CVT)[71] was employed to locate the optimal free-energy bottleneck at each temperature. Quantum tunneling effects were accounted for using the microcanonical optimized multidimensional tunneling (μOMT) method,[72] which selects the dominant tunneling contribution from both small-curvature tunneling (SCT)[73] and large-curvature tunneling (LCT)[74] (restricted to the vibrational ground state) at each energy grid.

Electronic structure calculations were performed using Gaussian [16,75] while VTST/MT rate constant calculations were carried out using Polyrate 17[76] in combination with Gaussrate 17-B[77] program.

3. Results and Discussion

3.1. Structures and Energetics

Figure 1 shows the optimized geometries of the Criegee intermediates CH_2OO, CCl_2OO, and CF_2OO, whereas Figures 2 and 3 depict the alcohol-forming transition states for their reactions with methane and ethane, respectively. All transition states exhibit incipient C–H bond cleavage in the alkane and partial O–O bond breaking in the Criegee species. Intrinsic reaction coordinate (IRC) calculations confirm a concerted but highly asynchronous insertion mechanism: immediately after the transition state, an O–H bond is formed, followed by the attachment of the newly formed OH group to the carbon atom from which hydrogen was abstracted. These computed structures show good agreement with previous studies.[47,78,79] Additional optimized structures are provided in the Supplementary Materials.

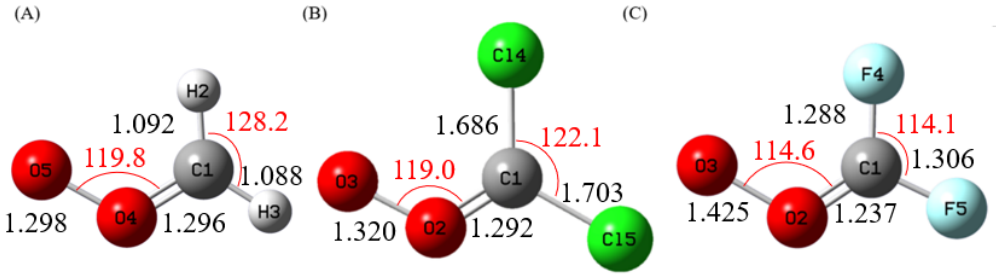

Figure 1. Calculated Geometries of (A) CH_2OO, (B) CCl_2OO, and (C) CF_2OO at MP2/aug-cc-pVDZ level. The Bond Lengths (black) are in Angstroms, and Bond Angles (red) are in Degrees.

 doi:10.20944/preprints202511.2205.v1

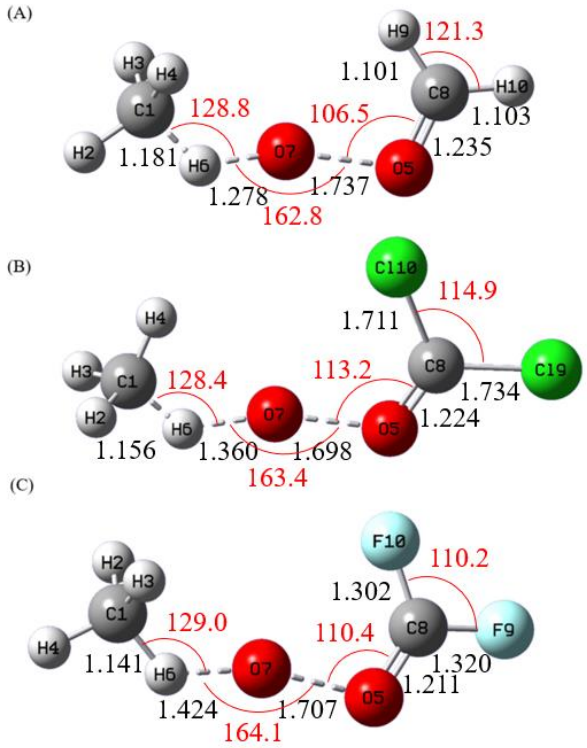

Figure 2. Calculated Transition State Geometries of (A) CH_2OO, (B) CCl_2OO, and (C) CF_2OO with CH_4 at MP2/aug-cc-pVDZ level. The Bond Lengths (black) are in Angstroms, and Bond Angles (red) in Degrees.

 doi:10.20944/preprints202511.2205.v1

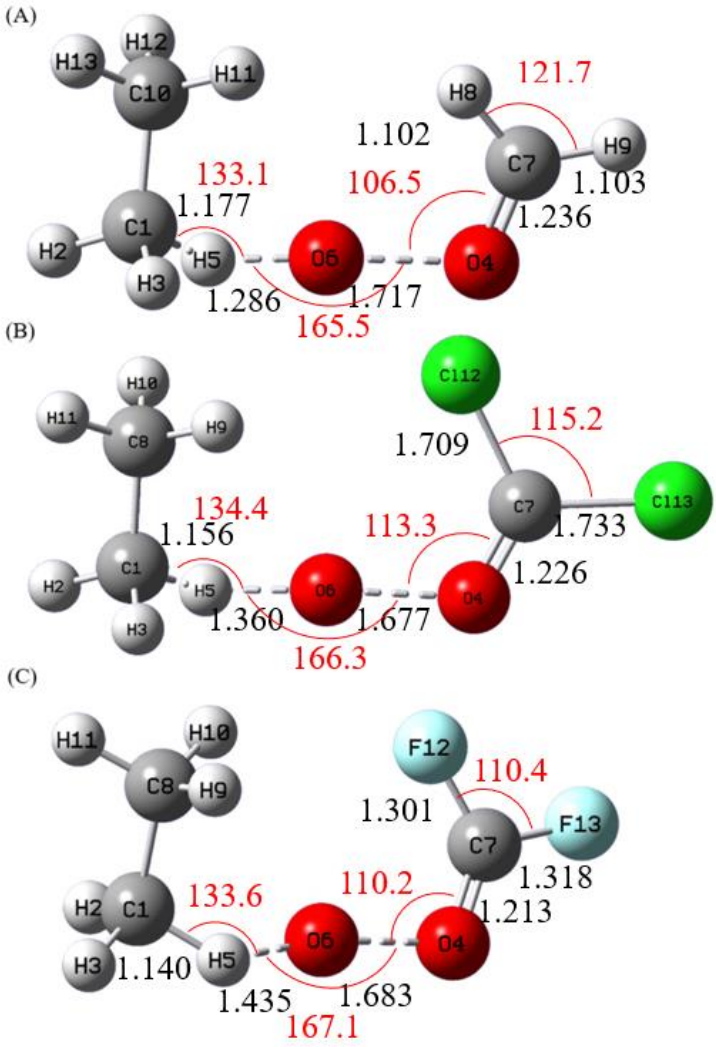

Figure 3. Calculated Transition State Geometries of (A) CH_2OO, (B) CCl_2OO, and (C) CF_2OO with C_2H_6 at MP2/aug-cc-pVDZ level. The Bond Lengths (black) are in Angstroms, and Bond Angles (red) in Degrees.

The reaction energy profiles are presented in Figures 4 and 5 for the methane and ethane reactions, respectively. For $CH_2OO + CH_4$ (Figure 4), the Born–Oppenheimer barrier heights are 24.6, 16.4, and 8.5 kcal/mol for CH_2OO, CCl_2OO, and CF_2OO, respectively, with corresponding reaction energies of −84.9, −101.4, and −112.5 kcal/mol. Thus, halogen substitution substantially lowers the barrier and increases the reaction exothermicity. The same trend is observed for the ethane reactions (Figure 5), where all barriers are 2–3 kcal/mol lower than those for methane. The barrier for $CF_2OO + C_2H_6$ is as small as 6.5 kcal mol^{-1}. The current barrier heights are 2–5 kcal/mol higher than those reported by Xu *et al.*,[47] who used lower-level electronic structure methods.

 doi:10.20944/preprints202511.2205.v1

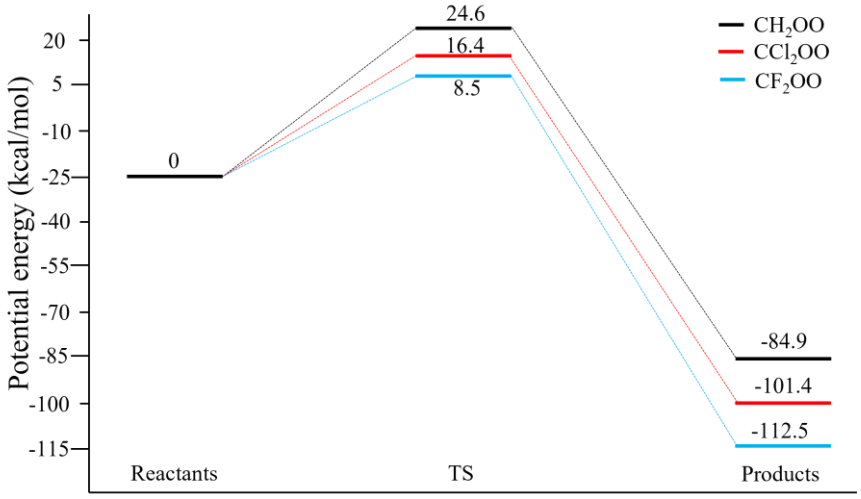

Figure 4. Calculated Potential Energy Profile of $CX_2OO + CH_4$ (X = H, Cl, F) at CCSD(T)/CBS//MP2/aug-cc-pVDZ Level.

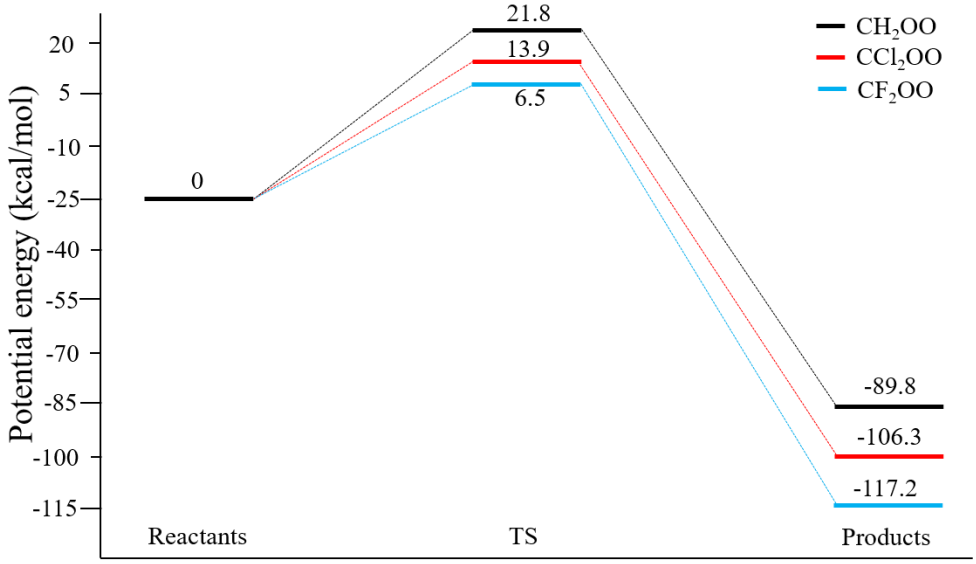

Figure 5. Calculated Potential Energy Profile of $CX_2OO + C_2H_6$ (X = H, Cl, F) at CCSD(T)/CBS//MP2/aug-cc-pVDZ Level.

These energetic trends are consistent with structural changes induced by halogen substitution. As seen in Figure 1, replacing H with Cl or F shortens the carbonyl C=O bond and weakens the peroxidic O–O bond. The O–O bond strengths were calculated to be 58.3, 41.8, and 30.9 kcal/mol for CH_2OO, CCl_2OO, and CF_2OO, respectively. The systematic weakening of the O–O bond directly accounts for the reduction in insertion barriers upon halogen substitution, consistent with the trend in calculated bond dissociation energies. The stronger product stabilization also contributes to increasingly exothermic reaction energies upon halogenation, reflecting the greater thermodynamic stability of CX_2O (X = H, Cl, F). Energetics for partially halogenated formaldehyde oxides show similar trends and are provided in the Supplementary Materials.

3.2. Rate Constants of $CH_2OO + CH_4$

All rate constants discussed below are based on the dual-level VTST/MT calculations. Table 1 lists the computed rate constants, and Figure 6 shows the corresponding Arrhenius plot. Because this reaction has a relatively high barrier, the rate constant at 300 K is only on the order of 10^{-29} cm^3 $molecule^{-1}$ s^{-1}. Despite the small magnitude, tunneling effects are substantial. At 300 K, tunneling

 doi:10.20944/preprints202511.2205.v1

enhances the CVT rate constant by a factor of about 3, and the enhancement reaches two orders of magnitude at 200 K. As seen in Figure 6, the Arrhenius curve displays pronounced curvature below 250 K and becomes nearly temperature independent below ~150 K, characteristic of tunneling-dominated kinetics.

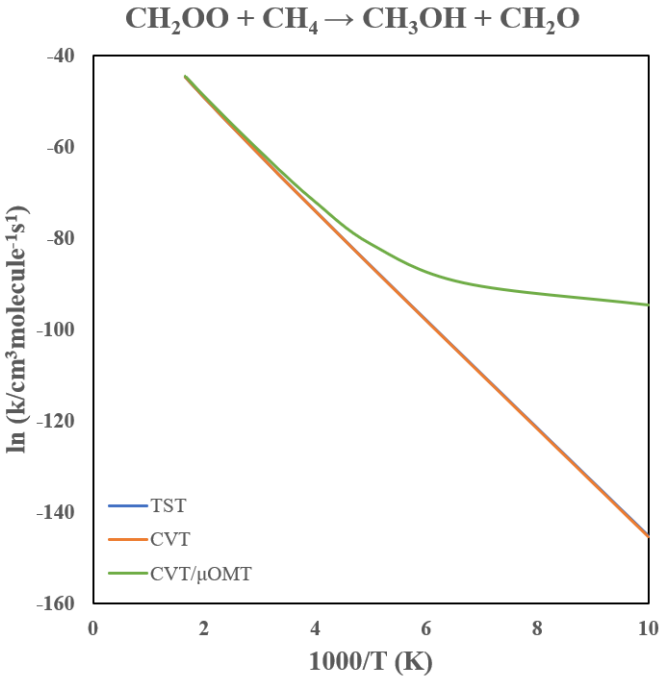

Figure 6. Arrhenius Plot of the $CH_2OO + CH_4 \rightarrow CH_2O + CH_3OH$ Rate Constants.

Table 1. Calculated Rate Constants (in cm^3 $molecule^{-1}$ s^{-1}) for the $CH_2OO + CH_4 \rightarrow CH_2O + CH_3OH$ Reaction.

T(K)	TST	CVT	CVT/μOMT
100	8.29×10^{-64}	6.33×10^{-64}	7.65×10^{-42}
150	1.06×10^{-46}	8.99×10^{-47}	9.97×10^{-40}
200	4.55×10^{-38}	4.06×10^{-38}	5.12×10^{-36}
250	7.91×10^{-33}	7.25×10^{-33}	5.43×10^{-32}
298.15	2.11×10^{-29}	1.97×10^{-29}	6.31×10^{-29}
300	2.73×10^{-29}	2.54×10^{-29}	7.98×10^{-29}
350	9.87×10^{-27}	9.30×10^{-27}	1.97×10^{-29}
400	8.66×10^{-25}	8.22×10^{-25}	1.40×10^{-24}
500	5.09×10^{-22}	4.88×10^{-22}	6.65×10^{-22}
600	3.97×10^{-20}	3.83×10^{-20}	4.67×10^{-20}

The origin of this strong tunneling behavior can be traced to the hydrogen-atom transfer step: the terminal oxygen of CH_2OO abstracts an H atom from methane before the newly formed OH group attaches to carbon. All nuclear motions involved in this step are confined to a very limited spatial region, resulting in a narrow tunneling barrier. The classical and vibrationally adiabatic reaction-path energies (V_{MEP} and V_a^G) are shown in Figure 7, together with the corresponding zero-point energies (ZPE). The ZPE decreases by 1.2 kcal/mol from reactants to the transition state, resulting in an effectively lower barrier height along the V_a^G surface. The variational effect of this reaction is relatively small because the reaction bottleneck remains close to the transition state due to the high barrier. Accordingly, the CVT and TST values remain similar across the entire temperature range.

 doi:10.20944/preprints202511.2205.v1

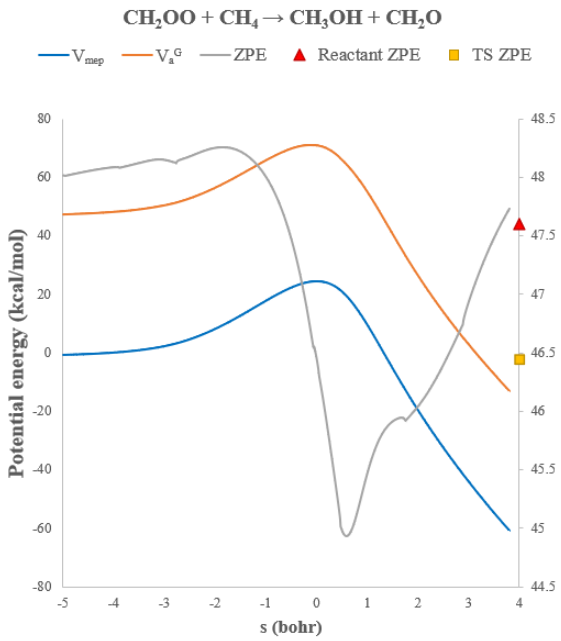

Figure 7. Potential energies (V_{MEP} and V_a^G, left axis) and vibrational zero-point energies (ZPE, right axis) along the reaction path for $CH_2OO + CH_4 \rightarrow CH_2O + CH_3OH$.

3.3. Rate Constants of $CH_2OO + C_2H_6$

Table 2 summarizes the calculated rate constants, and Figure 8 shows the Arrhenius plot. Compared with the methane reaction, the TST rate constants near 300 K increase by roughly a factor of 20, consistent with the 2.8 kcal/mol lower barrier predicted for ethane. Despite this reduced barrier, tunneling remains comparably important: at 300 K and 200 K, tunneling enhances the rate constants by factors of approximately 3 and 100, respectively. The strong curvature in the Arrhenius behavior below 250 K again signals dominant tunneling contributions, mirroring the behavior observed for methane.

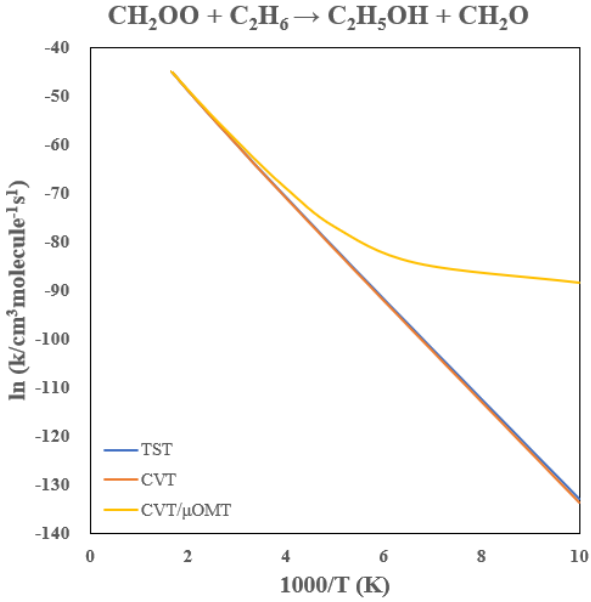

Figure 8. Arrhenius Plot of the $CH_2OO + C_2H_6 \rightarrow CH_2O + C_2H_5OH$ Rate Constants.

Table 2. Calculated Rate Constants (in cm^3 $molecule^{-1}$ s^{-1}) for the $CH_2OO + C_2H_6 \rightarrow CH_2O + C_2H_5OH$ Reaction.

 doi:10.20944/preprints202511.2205.v1

T(K)	TST	CVT	CVT/μOMT
100	3.62×10^{-58}	2.02×10^{-58}	8.85×10^{-39}
150	2.70×10^{-43}	1.98×10^{-43}	5.01×10^{-37}
200	9.10×10^{-36}	7.60×10^{-36}	8.68×10^{-34}
250	3.48×10^{-31}	3.12×10^{-31}	2.60×10^{-30}
298.15	3.52×10^{-28}	3.28×10^{-28}	1.15×10^{-27}
300	4.40×10^{-28}	4.11×10^{-28}	1.41×10^{-27}
350	7.82×10^{-26}	7.49×10^{-26}	1.69×10^{-25}
400	4.03×10^{-24}	3.93×10^{-24}	6.92×10^{-24}
500	1.14×10^{-21}	1.12×10^{-21}	1.52×10^{-21}
600	5.44×10^{-20}	5.42×10^{-20}	6.43×10^{-20}

The variational contributions are modest in this case as well. Above 250 K, the CVT correction reduces the TST value by < 10%. Thus, for both methane and ethane, the CH_2OO insertion chemistry proceeds through a hydrogen-transfer-dominated mechanism in which quantum tunneling is the primary origin of the observed low-temperature reactivity.

3.4. Rate Constants of $CCl_2OO + CH_4$

The calculated rate constants for the $CCl_2OO + CH_4$ reaction are presented in Table 3, with the Arrhenius plot shown in Figure 9. Chlorination lowers the reaction barrier by 8.2 kcal/mol relative to CH_2OO, leading to a dramatic enhancement in reactivity: the predicted rate constant at 300 K is 10^{-23} cm^3 $molecule^{-1}$ s^{-1}, approximately six orders of magnitude larger than the unsubstituted case.

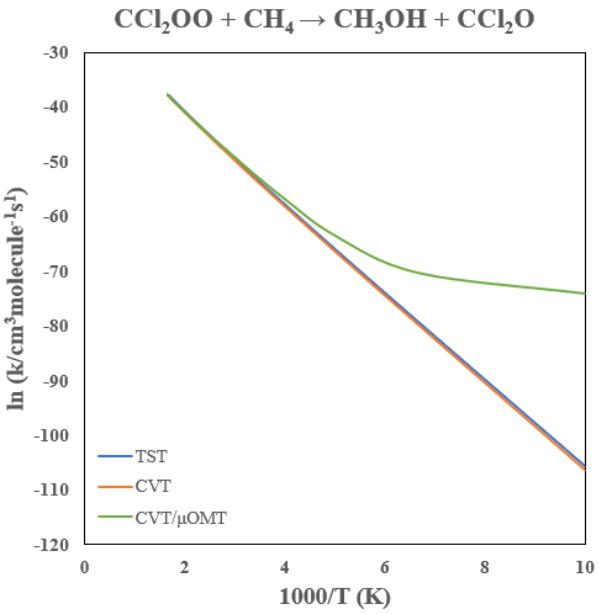

Figure 9. Arrhenius Plot of the $CCl_2OO + CH_4 \rightarrow CCl_2O + CH_3OH$ Rate Constants.

Table 3. Calculated Rate Constants (in cm^3 $molecule^{-1}$ s^{-1}) for the $CCl_2OO + CH_4 \rightarrow CCl_2O + CH_3OH$ Reaction.

T(K)	TST	CVT	CVT/μOMT
100	1.30×10^{-46}	6.91×10^{-47}	6.01×10^{-33}
150	3.80×10^{-35}	2.22×10^{-35}	2.71×10^{-31}
200	2.48×10^{-29}	1.52×10^{-29}	2.69×10^{-28}
250	8.74×10^{-26}	5.53×10^{-26}	2.22×10^{-25}
298.15	1.87×10^{-23}	1.21×10^{-23}	2.90×10^{-23}

 doi:10.20944/preprints202511.2205.v1

300	2.23×10^{-23}	1.44×10^{-23}	3.40×10^{-23}
350	1.25×10^{-21}	8.19×10^{-22}	1.49×10^{-21}
400	2.72×10^{-20}	1.80×10^{-20}	2.80×10^{-20}
500	2.28×10^{-18}	1.53×10^{-18}	2.00×10^{-18}
600	4.85×10^{-17}	3.28×10^{-17}	3.95×10^{-17}

Tunneling remains important despite the reduced barrier. At 300 K and 200 K, tunneling enhances the CVT rate constant by factors of 2.4 and 18, respectively, with pronounced curvature in the Arrhenius behavior below ~200 K. In contrast to $CH_2OO + CH_4$, the variational contribution becomes more significant. The CVT correction lowers the TST rate constant by ~35–40% at 300–200 K, reflecting a shift of the reaction bottleneck away from the saddle point. As the barrier becomes smaller and broader, tunneling and variational effects coexist, while tunneling still dominates the low-temperature kinetics.

3.5. Rate Constants of $CCl_2OO + C_2H_6$

Table 4 provides the calculated rate constants for the $CCl_2OO + C_2H_6$ reaction, and Figure 10 illustrates the Arrhenius plot. Chlorination lowers the reaction barrier by 7.8 kcal/mol, yielding a 300 K rate constant near 10^{-22} cm^3 $molecule^{-1}$ s^{-1}, roughly five orders of magnitude higher than the corresponding CH_2OO reaction and comparable to the chlorinated methane case above.

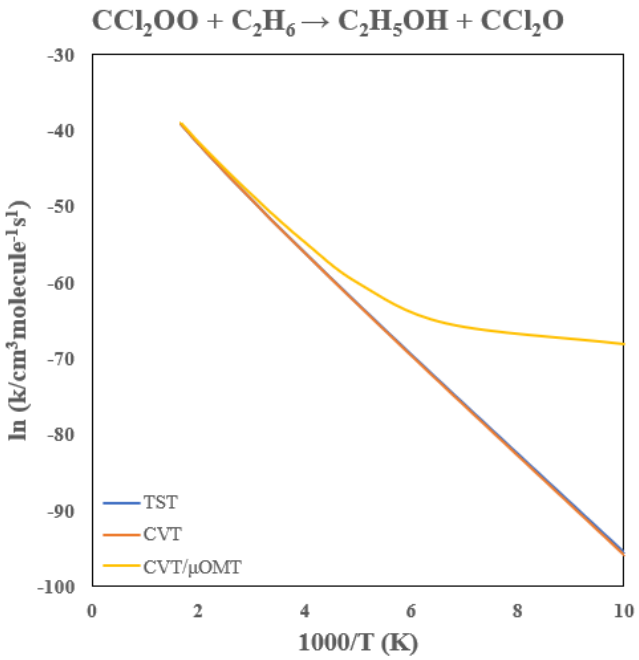

Figure 10. Arrhenius Plot of the $CCl_2OO + C_2H_6 \rightarrow CCl_2O + C_2H_5OH$ Rate Constants.

Table 4. Calculated Rate Constants (in cm^3 $molecule^{-1}$ s^{-1}) for the $CCl_2OO + C_2H_6 \rightarrow CCl_2O + C_2H_5OH$ Reaction.

T(K)	TST	CVT	CVT/μOMT
100	6.40×10^{-42}	4.46×10^{-42}	5.72×10^{-30}
150	1.67×10^{-32}	1.39×10^{-32}	8.50×10^{-29}
200	1.05×10^{-27}	9.51×10^{-28}	1.73×10^{-26}
250	9.25×10^{-25}	8.73×10^{-25}	3.70×10^{-24}
298.15	8.14×10^{-23}	7.88×10^{-23}	1.93×10^{-22}
300	9.41×10^{-23}	9.12×10^{-23}	2.20×10^{-22}
350	2.76×10^{-21}	2.72×10^{-21}	4.91×10^{-21}

 doi:10.20944/preprints202511.2205.v1

400	3.70×10^{-20}	3.67×10^{-20}	5.59×10^{-20}
500	1.58×10^{-18}	1.58×10^{-18}	1.95×10^{-18}
600	2.16×10^{-17}	2.16×10^{-17}	2.45×10^{-17}

Tunneling enhancements mirror those of the methane reaction, increasing the rate constant by roughly factors of 2.4 and 18 at 300 K and 200 K, respectively. The variational correction is modest above 200 K, reducing TST values by <10%. Thus, similar to the methane system, chlorination significantly accelerates CI reactivity with ethane, while tunneling remains a persistent contributor to the rate enhancement under atmospheric and especially low-temperature conditions.

3.6. Rate Constants of $CF_2OO + CH_4$

The predicted rate constants for the $CF_2OO + CH_4$ reaction are listed in Table 5 and plotted in Figure 11. The V_{MEP}, V_a^G, and ZPE curves are plotted in Figure 12. Fluorination has an even more dramatic effect than chlorination, lowering the barrier by 16.1 kcal/mol. As a result, the 300 K rate constant reaches ~10^{-17} cm^3 $molecule^{-1}$ s^{-1}, approximately twelve orders of magnitude higher than that of CH_2OO.

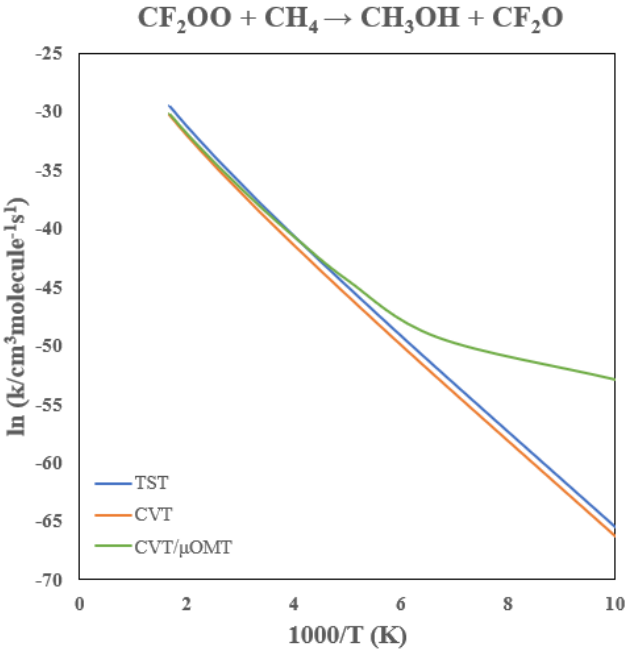

Figure 11. Arrhenius Plot of the $CF_2OO + CH_4 \rightarrow CF_2O + CH_3OH$ Rate Constants.

 doi:10.20944/preprints202511.2205.v1

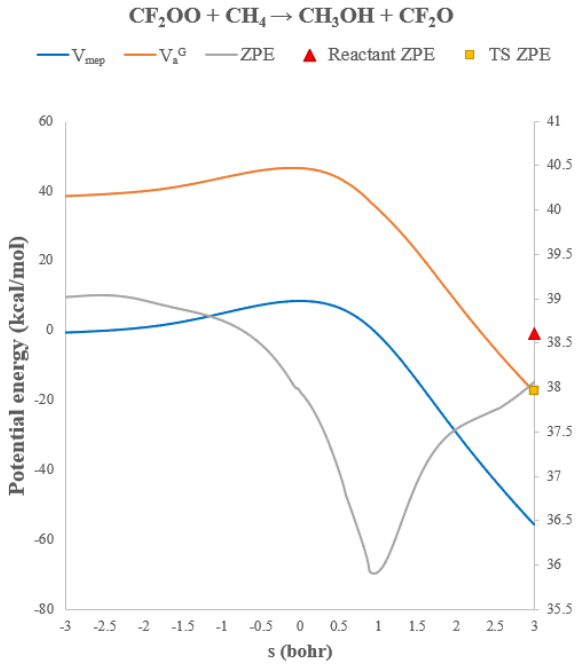

Figure 12. Potential energies (V_{MEP} and V_a^G, left axis) and vibrational zero-point energies (ZPE, right axis) along the reaction path for $CF_2OO + CH_4 \rightarrow CF_2O + CH_3OH$.

Table 5. Calculated Rate Constants (in cm^3 $molecule^{-1}$ s^{-1}) for the $CF_2OO + CH_4 \rightarrow CF_2O + CH_3OH$ Reaction.

T(K)	TST	CVT	CVT/μOMT
100	3.56×10^{-29}	1.58×10^{-29}	1.08×10^{-23}
150	2.69×10^{-23}	1.25×10^{-23}	4.06×10^{-22}
200	2.87×10^{-20}	1.37×10^{-20}	5.26×10^{-20}
250	2.15×10^{-18}	1.04×10^{-18}	2.19×10^{-18}
298.15	3.84×10^{-17}	1.87×10^{-17}	3.05×10^{-17}
300	4.21×10^{-17}	2.06×10^{-17}	3.33×10^{-17}
350	3.78×10^{-16}	1.86×10^{-16}	2.61×10^{-16}
400	2.07×10^{-15}	1.03×10^{-15}	1.32×10^{-15}
500	2.50×10^{-14}	1.25×10^{-14}	1.45×10^{-14}
600	1.47×10^{-14}	7.35×10^{-14}	8.14×10^{-14}

Because the barrier is so small, tunneling effects are less prominent relative to the chlorinated and unsubstituted cases. Tunneling enhances the rate constant by only factors of 1.6 and 3.8 at 300 K and 200 K, respectively, although noticeable curvature remains below ~150 K, where tunneling can increase the rate by over an order of magnitude. Interestingly, variational effects become more important here than in the CH_2OO system. The classical barrier is sufficiently shallow that the optimal dividing surface shifts away from the transition state. CVT reduces the TST rate constant by ~50% across 200–600 K. Notably, the predicted 300 K rate constant is comparable to that of the OH + CH_4 reaction (~10^{-15} cm^3 $molecule^{-1}$ s^{-1}),[80-82] suggesting that CF_2OO could act as a minor methane sink during nighttime or low-[OH] atmospheric conditions.

3.7. Rate Constants of $CF_2OO + C_2H_6$

Table 6 summarizes the rate constants for the $CF_2OO + C_2H_6$ reaction, with the Arrhenius behavior shown in Figure 13. Fluorination lowers the barrier by 15.3 kcal/mol, yielding a 300 K rate

 doi:10.20944/preprints202511.2205.v1

constant near 10 ^{17} cm^3 molecule ^{1} s ^{1}, again about ten orders of magnitude larger than the unsubstituted CH_2OO system and comparable to the $CF_2OO + CH_4$ reaction.

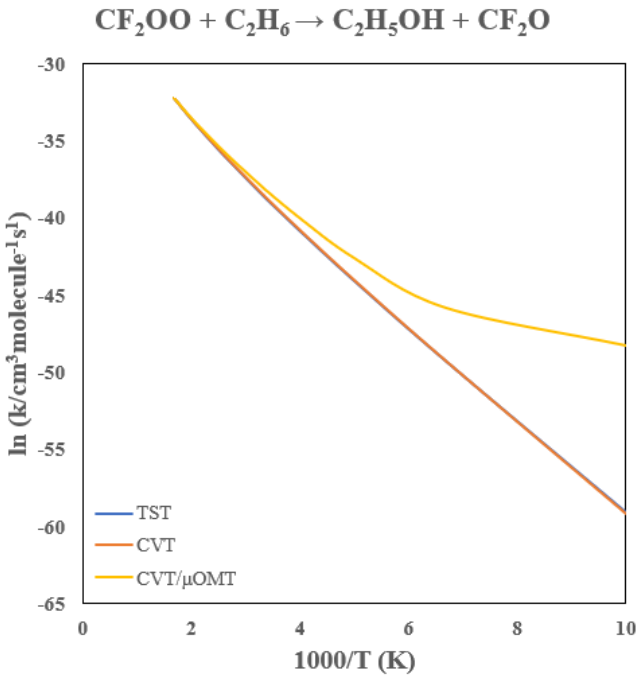

Figure 13. Arrhenius Plot of the $CF_2OO + C_2H_6 \rightarrow CF_2O + C_2H_5OH$ Rate Constants.

Table 6. Calculated Rate Constants (in cm^3 molecule^{-1} s^{-1}) for the $CF_2OO + C_2H_6 \rightarrow CF_2O + C_2H_5OH$ Reaction.

T(K)	TST	CVT	CVT/μOMT
100	4.55×10^{-26}	3.85×10^{-26}	2.10×10^{-21}
150	8.54×10^{-22}	8.09×10^{-22}	2.45×10^{-20}
200	1.47×10^{-19}	1.45×10^{-19}	6.00×10^{-19}
250	3.72×10^{-18}	3.72×10^{-18}	7.92×10^{-18}
298.15	3.31×10^{-17}	3.31×10^{-17}	5.20×10^{-17}
300	3.56×10^{-17}	3.56×10^{-17}	5.54×10^{-17}
350	1.92×10^{-16}	1.91×10^{-16}	2.50×10^{-16}
400	7.21×10^{-16}	7.12×10^{-16}	8.35×10^{-16}
500	5.16×10^{-15}	5.00×10^{-15}	5.19×10^{-15}
600	2.13×10^{-14}	2.03×10^{-14}	1.98×10^{-14}

Tunneling effects are modest due to the low barrier, increasing the CVT rate constant by factors of approximately 1.6 and 4.1 at 300 and 200 K, respectively, with notable tunneling curvature only below ~150 K. Variational effects are small, reducing the TST rate constants by < 5% above 200 K. Interestingly, while the barrier is lower for ethane than for methane, the room-temperature rates are nearly identical. This originates from the much larger pre-exponential factor in the methane reaction due to its higher symmetry and smaller rotational partition function. The symmetry number for the CH_4 reaction ($\sigma = 12$) is also twice that for ethane, making entropic factors important in determining the overall bimolecular rate.

3.8. Kinetic Isotope Effects

Kinetic isotope effects (KIEs) provide valuable mechanistic signatures for reactions that involve tunneling through a barrier. The reactions studied here involve transfer of either a hydrogen atom or a terminal oxygen atom from the Criegee intermediate to the alkane; therefore, both H/D and

 doi:10.20944/preprints202511.2205.v1

$^{16}O/^{18}O$ isotope substitutions can reveal the characteristics of the reaction mechanism and the extent to which tunneling shapes the dynamics.[72,73] It is often informative to factorize the KIEs into the translational, rotational, vibrational, variational, and tunneling contributions for analysis[83–85]:

$$\mathrm{KIE} = \frac{k_{\mathrm{H}}}{k_{\mathrm{D}}} = \eta_{\mathrm{trans}}\eta_{\mathrm{rot}}^{\neq}\eta_{\mathrm{vib}}^{\neq}\eta_{\mathrm{var}}\eta_{\mathrm{tunneling}}$$

where the first two contributions are temperature independent. Tables 7–10 list the predicted isotope effects and their decomposed contributions.

Table 7. Calculated Deuterium Kinetic Isotope Effects and Contributions of $CH_2OO + CH_4$ / $CH_2OO + CD_4$.

T(K)	TST	CVT	CVT/μOMT	η_{trans}	$\eta_{rot}^{\neq}$	$\eta_{vib}^{\neq}$	η_{var}	$\eta_{tunneling}$
100	10.4	9.34	1.95×10^3			3.63	0.897	209
150	5.39	5.06	159			1.88	0.939	31.4
200	3.80	3.64	10.7			1.32	0.958	2.95
250	3.04	2.95	3.91			1.06	0.969	1.33
298.15	2.61	2.55	2.84	1.27	2.26	0.909	0.976	1.12
300	2.60	2.53	2.82			0.904	0.976	1.11
350	2.31	2.26	2.37			0.803	0.980	1.05
400	2.10	2.03	2.11			0.731	0.984	1.02
500	1.82	1.80	1.80			0.635	0.989	0.998
600	1.65	1.64	1.62			0.575	0.991	0.991

Table 8. Calculated Deuterium Kinetic Isotope Effects and Contributions of $CH_2OO + C_2H_6$ / $CH_2OO + C_2D_6$.

T(K)	TST	CVT	CVT/μOMT	η_{trans}	$\eta_{rot}^{\neq}$	$\eta_{vib}^{\neq}$	η_{var}	$\eta_{tunneling}$
100	17.0	12.2	1.00×10^3			8.86	0.714	82.8
150	7.13	5.92	137.5			3.71	0.831	23.2
200	4.55	4.06	14.0			2.37	0.894	3.45
250	3.44	3.20	5.03			1.79	0.931	1.57
298.15	2.85	2.72	3.42	1.17	1.64	1.49	0.953	1.26
300	2.84	2.71	3.38			1.48	0.954	1.25
350	2.46	2.39	2.71			1.28	0.970	1.14
400	2.20	2.16	2.33			1.15	0.980	1.08
500	1.88	1.87	1.91			0.979	0.992	1.02
600	1.69	1.68	1.68			0.878	0.998	0.999

Table 9. Calculated Deuterium Kinetic Isotope Effects and Contributions of $CH_2{}^{16}O{}^{16}O + CH_4$ / $CH_2{}^{18}O{}^{18}O + CD_4$.

T(K)	TST	CVT	CVT/μOMT	η_{trans}	$\eta_{rot}^{\neq}$	$\eta_{vib}^{\neq}$	η_{var}	$\eta_{tunneling}$
100	1.23	1.24	6.40			1.13	1.00	5.18
150	1.16	1.16	4.57			1.07	0.999	3.94
200	1.12	1.12	2.09			1.03	0.998	1.87
250	1.10	1.10	1.35			1.01	0.997	1.23
298.15	1.08	1.08	1.19	1.03	1.05	0.997	0.997	1.10
300	1.08	1.08	1.19			0.997	0.997	1.10
350	1.07	1.07	1.14			0.987	0.997	1.06
400	1.06	1.06	1.11			0.980	0.997	1.04
500	1.06	1.05	1.08			0.971	0.998	1.03
600	1.05	1.05	1.07			0.967	0.998	1.02

 doi:10.20944/preprints202511.2205.v1

Table 10. Calculated Deuterium Kinetic Isotope Effects and Contributions of $CH_2{}^{16}O{}^{16}O + C_2H_6$ / $CH_2{}^{18}O{}^{18}O + C_2H_6$.

T(K)	TST	CVT	CVT/μOMT	η_{trans}	$\eta_{rot}^{\neq}$	$\eta_{vib}^{\neq}$	η_{var}	$\eta_{tunneling}$
100	1.23	1.27	10.1			1.11	1.04	7.91
150	1.16	1.19	5.84			1.05	1.03	4.92
200	1.12	1.14	2.15			1.01	1.02	1.89
250	1.10	1.11	1.42			0.991	1.01	1.27
298.15	1.08	1.09	1.24	1.05	1.06	0.978	1.01	1.14
300	1.08	1.09	1.24			0.977	1.01	1.14
350	1.07	1.08	1.17			0.968	1.01	1.08
400	1.06	1.07	1.13			0.961	1.01	1.06
500	1.06	1.06	1.09			0.953	1.00	1.03
600	1.05	1.05	1.08			0.948	1.00	1.02

3.8.1. Deuterium Kinetic Isotope Effects (H/D)

Tables 7 and 8 show that the $CH_2OO + CH_4$ and $CH_2OO + C_2H_6$ reactions both exhibit large deuterium KIEs that increase sharply with decreasing temperature. At room temperature, CVT/μOMT predicts KIEs of 2.84 for methane and 3.42 for ethane. Although these magnitudes are similar to typical hydrogen-transfer reactions, the decomposed contributions indicate strong tunneling control. The temperature dependence of the deuterium KIEs is primarily due to the tunneling contribution below room temperature, and is due to the vibrational contribution above room temperature. Interestingly, the vibrational contributions of the ethane reaction are significantly higher due to the zero-point energy effects. The temperature-independent rotational contributions are also important. The zero-point energy (ZPE) and tunneling effects make the rate constants of the unsubstituted reactions much higher than those of the deuterated reactions at low temperature. The calculated rate constants and Arrhenius plots of the isotopically substituted reactions are included in the Supplementary Materials.

At temperatures below 250 K, tunneling becomes the dominant contributor to the KIE, exceeding factors of 30 (CH_4) and 23 (C_2H_6) at 150 K. At 200 K, tunneling elevates the KIE to 10.7 for methane and 14.0 for ethane. Below ~150 K, the KIEs increase by two to three orders of magnitude, reflecting barrier penetration on a narrow tunneling path.

Notably, the variational contribution to the KIE is small for both reactions, showing that tunneling enhancement primarily originates from the transmission coefficient rather than shifts in the dynamical bottleneck. Therefore, these alcohol-forming reactions proceed by highly quantum-mechanical hydrogen transfer even when the overall rate is slow at room temperature. These results further suggest that accurate deuterium KIE calculations should explicitly account for tunneling contributions.

3.8.2. Heavy-Atom Kinetic Isotope Effects ($^{16}O/^{18}O$)

Because the forming O–H bond is accompanied by a concerted insertion of the terminal oxygen into the C–H bond, oxygen motion also contributes to the reaction coordinate. Tables 9 and 10 show that the ^{18}O KIE is close to unity at high temperature but grows as temperature decreases. For example, at 298 K, CVT/μOMT predicts ^{18}O KIEs of 1.19 (CH_4) and 1.24 (C_2H_6), while at 200 K, tunneling raises the KIE to 2.09 (CH_4) and 2.15 (C_2H_6). Such magnitudes are unusually large for heavy-atom substitution[86] and represent clear kinetic signatures of heavy-atom tunneling.[50,87–90] Evidence for oxygen tunneling in O–O bond activation and oxygen-transfer reactions has also been reported in peroxide bond cleavage and ozone-related rearrangements, further supporting the presence of heavy-atom tunneling in systems with weak or strained O–O linkages.[50,90] Heavy-atom tunneling is often masked experimentally due to competing reaction pathways and slow

 doi:10.20944/preprints202511.2205.v1

intrinsic kinetics, implying that these isotope effects may be most relevant for low-temperature modeling or laboratory studies employing cryogenic techniques rather than ambient experimental kinetics.

3.8.3. Mechanistic Implications

Together, the H/D and $^{16}O/^{18}O$ KIE data demonstrate that the reactions do not proceed only by classical over-the-barrier hydrogen abstraction. Both hydrogen and oxygen atoms participate in quantum tunneling through a constrained geometry. The transition state represents a concerted, asynchronous O-insertion process in which H and O motion are strongly coupled. These features reinforce the mechanistic picture derived from IRC results: the reaction path becomes narrow and steep at the point of O–H formation, creating favorable conditions for deep tunneling.

4. Summary

We have investigated the alcohol-forming reactions of CH_2OO and halogenated Criegee intermediates with methane and ethane using high-level electronic structure methods and variational transition state theory with multidimensional tunneling (VTST/MT). The reaction proceeds through a concerted but asynchronous insertion of the terminal oxygen atom into a C–H bond, with H/O motion coupled along the reaction coordinate. The results show that tunneling significantly enhances rate constants, especially below room temperature. Halogen substitution greatly accelerates reactivity, reducing barriers to < 10 kcal/mol for CCl_2OO and CF_2OO; fluorination increases 300 K rates by 10–12 orders of magnitude. CF_2OO reactions approach the reactivity of OH + CH_4, suggesting potential nighttime removal of light alkanes under low-[OH] conditions. Isotopic substitution reveals strong quantum signatures, with large H/D KIEs and unexpectedly strong ^{18}O KIEs, indicating coupled hydrogen–oxygen tunneling. These findings imply that halogenated Criegee intermediates, potentially generated from anthropogenic halogenated alkenes, may serve as low-temperature oxidants for alkanes and as minor sources of atmospheric alcohols. From a broader chemical perspective, the demonstrated tunneling-controlled insertion mechanism highlights opportunities for green oxidation strategies that exploit low-barrier oxygen transfer under mild or cryogenic conditions rather than high-temperature, energy-intensive industrial routes.

Ackowlegement: This work is supported by the National Science Council of Taiwan, grant number 113-2113-M-194-009.

References

1. Criegee, R. Mechanism of Ozonolysis. *Angew. Chem. Int. Ed. Engl.* **1975**, *14*, 745–752.
2. Johnson, D.; Marston, G. The Gas-Phase Ozonolysis of Unsaturated Volatile Organic Compounds in the Troposphere. *Chem. Soc. Rev.* **2008**, *37*, 699–716.
3. Vereecken, L.; Harder, H.; Novelli, A. The Reaction of Criegee Intermediates with NO, RO_2, and SO_2, and Their Fate in the Atmosphere. *Phys. Chem. Chem. Phys.* **2012**, *14*, 14682–14695.
4. Percival, C. J.; Welz, O.; Eskola, A. J.; Savee, J. D.; Osborn, D. L.; Topping, D. O.; Lowe, D.; Utembe, S. R.; Bacak, A.; McFiggans, G.; Cooke, M. C.; Xiao, P.; Archibald, A. T.; Jenkin, M. E.; Derwent, R. G.; Riipinen, I.; Mok, D. W. K.; Lee, E. P. F.; Dyke, J. M.; Taatjes, C. A.; Shallcross, D. E. Regional and Global Impacts of Criegee Intermediates on Atmospheric Sulphuric Acid Concentrations and First Steps of Aerosol Formation. *Faraday Discuss.* **2013**, *165*, 45–73.
5. Kurtén, T.; Lane, J. R.; Jørgensen, S.; Kjaergaard, H. G. A Computational Study of the Oxidation of SO_2 to SO_3 by Gas-Phase Organic Oxidants. *J. Phys. Chem. A* **2011**, *115*, 8669–8681.
6. Ziemann, P. J.; Atkinson, R. Kinetics, Products, and Mechanisms of Secondary Organic Aerosol Formation. *Chem. Soc. Rev.* **2012**, *41*, 6582–6605.
7. Gong, Y.; Chen, Z. Quantification of the Role of Stabilized Criegee Intermediates in the Formation of Aerosols in Limonene Ozonolysis. *Atmospheric Chem. Phys.* **2021**, *21*, 813–829.

 doi:10.20944/preprints202511.2205.v1

8. Gutbrod, R.; Kraka, E.; Schindler, R. N.; Cremer, D. Kinetic and Theoretical Investigation of the Gas-Phase Ozonolysis of Isoprene: Carbonyl Oxides as an Important Source for OH Radicals in the Atmosphere. *J. Am. Chem. Soc.* **1997**, *119*, 7330–7342.
9. Novelli, A.; Vereecken, L.; Lelieveld, J.; Harder, H. Direct Observation of OH Formation from Stabilised Criegee Intermediates. *Phys. Chem. Chem. Phys.* **2014**, *16*, 19941–19951.
10. Long, B.; Bao, J. L.; Truhlar, D. G. Atmospheric Chemistry of Criegee Intermediates: Unimolecular Reactions and Reactions with Water. *J. Am. Chem. Soc.* **2016**, *138*, 14409–14422.
11. Long, B.; Wang, Y.; Xia, Y.; He, X.; Bao, J. L.; Truhlar, D. G. Atmospheric Kinetics: Bimolecular Reactions of Carbonyl Oxide by a Triple-Level Strategy. *J. Am. Chem. Soc.* **2021**, *143*, 8402–8413.
12. Chao, W.; Hsieh, J.-T.; Chang, C.-H.; Lin, J. J.-M. Direct Kinetic Measurement of the Reaction of the Simplest Criegee Intermediate with Water Vapor. *Science* **2015**, *347*, 751–754.
13. Smith, M. C.; Chang, C.-H.; Chao, W.; Lin, L.-C.; Takahashi, K.; Boering, K. A.; Lin, J. J.-M. Strong Negative Temperature Dependence of the Simplest Criegee Intermediate CH_2OO Reaction with Water Dimer. *J. Phys. Chem. Lett.* **2015**, *6*, 2708–2713.
14. Vereecken, L. The Reaction of Criegee Intermediates with Acids and Enols. *Phys. Chem. Chem. Phys.* **2016**, *18*, 21–46.
15. Tratnyek, P. G.; Edwards, E.; Carpenter, L.; Blossom, S. Environmental Occurrence, Fate, Effects, and Remediation of Halogenated (Semi)Volatile Organic Compounds. *Environ. Sci. Process. Impacts* **2020**, *22*, 465–471.
16. U.S. EPA. Technical Overview of Volatile Organic Compounds (VOCs); *U.S. Environmental Protection Agency: Washington, DC*, **2023**.
17. Varga, B.; Csenki, J. T.; Tóth, B. L.; Béke, F.; Novák, Z.; Kotschy, A. Application of Industrially Relevant HydroFluoroOlefin (HFO) Gases in Organic Syntheses. *Synthesis* **2021**, *53*, 4313-4326**.**
18. Ceballos, D. M.; Fellows, K.; Evans, A. E.; Janulewicz, P. A.; Lee, E. G.; Whittaker, S. G. Perchloroethylene and Dry Cleaning: It's Time to Move the Industry to Safer Alternatives. *Front. Public Health* **2021**, *9*, 638082.
19. Modenese, A.; Bisegna, F.; Fabbri, G.; Cozza, V. Evaluation of Occupational Exposure to Perchlorethylene in the Dry-Cleaning Industry. *Int. J. Environ. Res. Public Health* **2019**, *16*, 2832.
20. Tanaka, K.; Higashi, Y. Thermodynamic Properties of HFO-1234yf (2,3,3,3-Tetrafluoropropene). *Int. J. Refrigeration* **2010**, *33*, 474-479.
21. Puts, G. J.; Crouse, P.; Ameduri, B. M. Polytetrafluoroethylene: Synthesis and Characterization of the Original Extreme Polymer. *Chem. Rev.* **2019**, *119*, 1763-1805.
22. Kumar, A.; Kumar, S.; Mall, A. A Comprehensive Review Regarding Condensation of Low-GWP Refrigerants (Including R-1234yf, R-1234ze) in HVAC Systems. *Processes* **2022**, *10*, 1882.
23. Zhang, X.; Li, Y. A Review of Recent Research on Hydrofluoroolefin (HFO) and Hydrochlorofluoroolefin (HCFO) Refrigerants. *Energy* **2024**, *311*, 133423.
24. Caravan, R. L.; Vansco, M. F.; Lester, M. I. *Open questions on the reactivity of Criegee intermediates.* Commun. Chem. **2021**, 4, 44.
25. Karlsson, E.; Rabayah, R.; Liu, T.; Cruz, E. M.; Kozlowski, M. C.; Karsili, T. N. V.; Lester, M. I. Electronic Spectroscopy of the Halogenated Criegee Intermediate, ClCHOO: Experiment and Theory. *J. Phys. Chem. A* **2024**, *128*, 10949-10956.
26. Taatjes, C. A.; Shallcross, D. E.; Percival, C. J. Research frontiers in the chemistry of Criegee intermediates and tropospheric ozonolysis. *Phys. Chem. Chem. Phys.* **2014**, *16*, 1704-1718.
27. Welz, O.; Savee, J. D.; Osborn, D. L.; Vasu, S.; Reisenauer, H. P.; Lester, M. I.; Taatjes, C. A. Direct Kinetic Measurements of Criegee Intermediate (CH_2OO) Formed by Reaction of CH_2I with O_2. *Science* **2012**, *335*, 204-207.
28. Novelli, A.; Vereecken, L.; Lelieveld, J.; Harder, H. Direct Observation of OH Formation from Stabilised Criegee Intermediates. *Phys. Chem.***2014**, *16*, 19941-19951.
29. Watson, N. A. I.; Beames, J. M. Bimolecular Sinks of Criegee Intermediates Derived from Hydrofluoroolefins — A Computational Analysis. *Environ. Sci.: Atmos*. **2023**, *3*, 1460-1484.
30. Holland, R. E. T.; Khan, M. A. H.; Driscoll, I.; Chhantyal-Pun, R.; Derwent, R. G.; Taatjes, C. A.; Orr-Ewing, A. J.; Percival, C. J.; Shallcross, D. E. Investigation of the Production of Trifluoroacetic Acid from Two

 doi:10.20944/preprints202511.2205.v1

Halocarbons, HFC-134a and HFO-1234yf, and Its Fates Using a Global 3-D Chemical Transport Model. *ACS Earth Space Chem.* **2021**, *5*, 849-857.

31. McGillen, M. R.; Fried, Z. T. P.; Khan, M. A. H.; Zhang, K. Z. Ozonolysis Can Produce Long-Lived Greenhouse Gases from Commercial Refrigerants. *Proc. Natl. Acad. Sci. U.S.A.* **2023**, *120*, e2312714120.
32. Hearn, J. D.; Harding, L. B.; Sheps, L.; et al. Electronic Spectroscopy of the Halogenated Criegee Intermediates: Photochemical Generation and VUV Photoionization Detection of ClCHOO. *J. Phys. Chem. A* **2024**, *128*, 10949-10956.
33. Welz, O.; Savee, J. D.; Osborn, D. L.; Vasu, S. S.; Percival, C. J.; Shallcross, D. E.; Taatjes, C. A. Direct Kinetic Measurements of Criegee Intermediate (CH_2OO) Formed by Reaction of CH_2I with O_2. *Science* **2012**, *335*, 204-207.
34. Ting, W. L.; Chang, C. H.; Chao, W.; Smith, M. C.; Lin, J. J. M. Direct Kinetic Measurement of the Reaction of the Simplest Criegee Intermediate CH_2OO with Water Vapor. *J. Phys. Chem. A* **2014**, *118*, 10116-10125.
35. Lee, Y.-P. Perspective: Spectroscopy and kinetics of small gaseous Criegee intermediates. *J. Chem. Phys.* **2015**, *143*, 020901.
36. Taatjes, C. A. Criegee intermediates: what direct production and detection can teach us about reactions of carbonyl oxides. *Annu. Rev. Phys. Chem.* **2017**, *68*, 183-207.
37. Gong, S.; Shi, Y. Evaluation of Comprehensive Monthly-Gridded Methane Emissions from Natural and Anthropogenic Sources in China. *Sci. Total Environ.* **2021**, *784*, 147116.
38. Lee, B. H.; Munger, W.; Wofsy, S. C.; Goldstein, A. H. Anthropogenic emissions of nonmethane hydrocarbons in the United States: Measured seasonal variations from 1992–1996 and 1999–2001 *J. Geophys. Res. Atmos.* **2006**, *111*, D20307.
39. Peischl, J.; Ryerson, T. B.; Aikin, K. C.; et al. Quantifying Methane and Ethane Emissions to the Atmosphere from Central and Western U.S. Oil and Gas Production Regions. *J. Geophys. Res. Atmos.* **2018**, *123*, 7725-7740.
40. Allen, D. T.; Torres, V. M.; Thomas, J.; Sullivan, D. W.; Harrison, M.; Hendler, A.; Herndon, S. C.; Kolb, C. E.; Fraser, M. P.; Hill, A. D.; Lamb, B. Attributing Atmospheric Methane to Anthropogenic Emission Sources. *Acc. Chem. Res.***2016**, *49*, 1494-1502.
41. Bourtsoukidis, E.; et al. Non-methane hydrocarbon (C_2–C_8) sources and sinks in and around the Arabian Gulf. *Atmos. Chem. Phys.* **2019**, *19*, 7209-7232.
42. Li, M.; Pozzer, A.; Lelieveld, J.; Williams, J. Northern hemispheric atmospheric ethane trends (2006–2016) with reference to methane and propane. *Earth Syst. Sci. Data* **2022**, *14*, 4351-4364.
43. Filonchyk, M.; Peterson, M. P.; Zhang, L.; Hurynovich, V.; He, Y. Greenhouse Gases Emissions and Global Climate Change: Examining the Influence of CO_2, CH_4, and N_2O. *Sci. Total Environ.* **2024**, *935*, 173359.
44. Dorofeenko, S. O.; Polianczyk, E. V.; Tsvetkov, M. V. Toward the Ultimate Efficiency of Methane to Syngas Conversion by Partial Oxidation: A Moving Bed Reactor with Parallel Preheating of Reactants. *Fuel* **2024**, *363*, 131005.
45. Rajeswari, S.; Baskaran, D.; Saravanan, P.; Rajasimman, M.; Rajamohan, N.; Vasseghian, Y. Production of Ethanol from Biomass – Recent Research, Scientometric Review and Future Perspectives. *Fuel* **2022**, *317*, 123448.
46. Gao, J.; Li, Z.; Dong, M.; Fan, W.; Wang, J. Thermodynamic Analysis of Ethanol Synthesis from Hydration of Ethylene Coupled with a Sequential Reaction. *Front. Chem. Sci. Eng.* **2020**, *14*, 847–856.
47. Xu, K.; Wang, W.; Wei, W.; Feng, W.; Sun, Q.; Li, P. Insights into the Reaction Mechanism of Criegee Intermediate CH_2OO with Methane and Implications for the Formation of Methanol. *J. Phys. Chem. A* **2017**, *121*, 7236–7245.
48. Schreiner, P. R. Quantum Mechanical Tunneling Is Essential to Understanding Chemical Reactivity. *Trends Chem.* **2020**, *2*, 980–989.
49. Cha, Y.; Murray, C. J.; Klinman, J. P. Hydrogen Tunneling in Enzyme Reactions. *Science* **1989**, *243*, 1325–1330.
50. Zhou, Y.; Fang, W.; Wang, L.; Zeng, X.; Zhang, D. H.; Zhou, M. Quantum Tunneling in Peroxide O–O Bond Breaking Reaction. *J. Am. Chem. Soc.* **2023**, *145*, 8817–8821.

 doi:10.20944/preprints202511.2205.v1

51. Truhlar, D. G.; Isaacson, A. D.; Garrett, B. C. In *Theory of Chemical Reaction Dynamics*; Baer, M., Ed.; CRC Press: Boca Raton, FL, **1985**; Vol. 4, p 65.
52. Truhlar, D. G.; Garrett, B. C. **Variational Transition-State Theory.** *Annu. Rev. Phys. Chem.* **1984**, *35*, 159–189.
53. Truhlar, D. G.; Garrett, B. C.; Klippenstein, S. J. Current Status of Transition-State Theory. *J. Phys. Chem.* **1996**, *100*, 12771–12800.
54. Fernandez-Ramos, A.; Ellingson, B. A.; Garrett, B. C.; Truhlar, D. G. Variational Transition State Theory with Multidimensional Tunneling. In *Reviews in Computational Chemistry*; Lipkowitz, K. B., Cundari, T. R., Eds.; Wiley-VCH: Hoboken, NJ, **2007**; Vol. 23, pp. 125–232.
55. Lu, D.-h.; Truong, T. N.; Melissas, V. S.; Lynch, G. C.; Liu, Y.-P.; Garrett, B. C.; Steckler, R.; Isaacson, A. D.; Rai, S. N.; Hancock, G. C.; Lauderdale, J. G.; Joseph, T.; Truhlar, D. G. POLYRATE 4: A New Version of a Computer Program for the Calculation of Chemical Reaction Rates for Polyatomics. *Comput. Phys. Commun.* **1992**, *71*, 235–262
56. Yu, T.; Truhlar, D. G. **Multipath Variational Transition State Theory: Multiple Reaction Paths and Path-Dependent Tunneling Effects.** *J. Phys. Chem. A* **2012**, *116*, 297–308.
57. Kohen, A. Kinetic Isotope Effects as Probes for Hydrogen Tunneling, Coupled Motion and Dynamics Contributions to Enzyme Catalysis. *Prog. React. Kinet. Mech.* **2003**, *28*, 119–156.
58. Sen, A.; Kohen, A. Enzymatic Tunneling and Kinetic Isotope Effects: Chemistry at the Crossroads. *J. Phys. Org. Chem.* **2010**, *23*, 613–619.
59. Møller, Chr.; Plesset, M. S. Note on an Approximation Treatment for Many-Electron Systems. *Phys. Rev.* **1934**, *46*, 618–622.
60. Woon, D. E.; Dunning, T. H. Gaussian Basis Sets for Use in Correlated Molecular Calculations. III. The Atoms Aluminum through Argon. *J. Chem. Phys.* **1993**, *98*, 1358–1371.
61. Dunning, T. H., Jr. Gaussian Basis Sets for Use in Correlated Molecular Calculations. I. The Atoms Boron through Neon and Hydrogen. *J. Chem. Phys.* **1989**, *90*, 1007–1023.
62. Helgaker, T.; Klopper, W.; Koch, H.; Noga, J. Basis-Set Convergence of Correlated Calculations on Water. *J. Chem. Phys.* **1997**, *106*, 9639–9646.
63. **Sorathia, K.; Frantzov, D.; Tew, D. P.** *Improved CPS and CBS Extrapolation of PNO-CCSD(T) Energies: The MOBH35 and ISOL24 Data Sets.* ***J. Chem. Theory Comput.*** **2024,** *20*, 2740–2750.
64. **Náfrádi, D.; Kállay, M.** *Self-consistent Basis Set Extrapolation of Hartree–Fock Energies.* ***Struct. Chem.*** **2025,** *36*, 1539–1546.
65. **Karton, A.** *Effective Basis Set Extrapolations for CCSDT, CCSDT(Q), and CCSDT(Q) Correlation Energies.* ***J. Chem. Phys.*** **2020,** *153*, 024102.
66. Page, M.; Doubleday, C.; McIver, J. W. Jr. Following steepest descent reaction paths. The use of higher energy derivatives with ab initio electronic structure methods. *J. Chem. Phys.* **1990**, *93*, 5634–5642.
67. Melissas, V. S.; Truhlar, D. G.; Garrett, B. C. Optimized Calculations of Reaction Paths and Reaction-Path Functions for Chemical Reactions. *J. Chem. Phys.* **1992**, *96*, 5758–5772.
68. Hu, W.-P.; Liu, Y.-P.; Truhlar, D. G. Variational Transition-State Theory and Semiclassical Tunnelling Calculations with Interpolated Corrections: A New Approach to Interfacing Electronic Structure Theory and Dynamics for Organic Reactions. *J. Chem. Soc. Faraday Trans.* **1994**, *90*, 1715.
69. Huang, C.-H.; You, R.-M.; Lian, P.-Y.; Hu, W.-P. Improved Interpolated Correction Schemes for Dual-Level Direct Dynamics Calculation. *J. Phys. Chem. A* **2000**, *104*, 7200–7208.
70. Corchado, J. C.; Espinosa-García, J.; Hu, W.-P.; Rossi, I.; Truhlar, D. G. Dual-Level Reaction-Path Dynamics (the III Approach to VTST with Semiclassical Tunneling). Application to $OH + NH_3 \rightarrow H_2O + NH_2$. *J. Phys. Chem.* **1995**, *99*, 687–694.
71. Truhlar, D. G.; Garrett, B. C. Variational Transition-State Theory. *Acc. Chem. Res.* **1980**, *13*, 440–448.
72. Liu, Y. P.; Lu, D. H.; Gonzalez-Lafont, A.; Truhlar, D. G.; Garrett, B. C. Direct Dynamics Calculation of the Kinetic Isotope Effect for an Organic Hydrogen-Transfer Reaction, Including Corner-Cutting Tunneling in 21 Dimensions. *J. Am. Chem. Soc.* **1993**, *115*, 7806–7817.

 doi:10.20944/preprints202511.2205.v1

73. Liu, Y. P.; Lynch, G. C.; Truong, T. N.; Lu, D. H.; Truhlar, D. G.; Garrett, B. C. Molecular modeling of the kinetic isotope effect for the [1,5]-sigmatropic rearrangement of cis-1,3-pentadiene. *J. Am. Chem. Soc.* **1993**, *115*, 2408–2415.
74. Fernandez-Ramos, A.; Truhlar, D. G. Improved algorithm for corner-cutting tunneling calculations. *J. Chem. Phys.* **2001**, *114*, 1491–1496.
75. **Frisch, M. J.; Trucks, G. W.; Schlegel, H. B.; et al.** *Gaussian 16, Revision B.01* Gaussian, Inc., Wallingford CT, 2016.
76. Zheng, J.; Bao, J. L.; Meana-Pañeda, R.; Zhang, S.; Lynch, B. J.; Corchado, J. C.; Chuang, Y.-Y.; Fast, P. L.; Hu, W.-P.; Liu, Y.-P.; Lynch, G. C.; Nguyen, K. A.; Jackels, C. F.; Fernandez Ramos, A.;Ellingson, B. A.; Melissas, V. S.; Villà, J. Rossi, I.; Coitiño, E. L.; Pu, J.; Albu, T. V.; Ratkiewicz, A.; Steckler, R.; Garrett, B. C.; Isaacson, A. D.; Truhlar, D. G. Polyrate-version 2017-C; *University of Minnesota: Minneapolis*, **2017**.
77. Zheng, J.; Bao, J. L.; Zhang, S.; Corchado, J. C.; Meana-Pañeda, R.; Chuang, Y.-Y.; Coitiño, E. L.; Ellingson, B. A.; Truhlar, D. G. *Gaussrate 17*; *University of Minnesota: Minneapolis*, **2017.**
78. Li, J.; Carter, S; Bowman, J. M.; Dawes R.; Xie, D.; Guo, H. High-Level, First-Principles, Full-Dimensional Quantum Calculation of the Ro-vibrational Spectrum of the Simplest Criegee Intermediate (CH_2OO). *J. Phys. Chem. Lett.* **2014**, *5*, 2364–2369.
79. Wagner, J. P. Gauging stability and reactivity of carbonyl O-oxide Criegee intermediates. *Phys. Chem. Chem. Phys.* **2019**, *21*, 21530.
80. Howard, C. J.; Evenson, K. M. Rate constants for the reactions of OH with CH_4 and fluorine, chlorine, and bromine substituted methanes at 296 K. *J. Chem. Phys.* **1976**, *64*, 197–202.
81. Berg, F.; Novelli, A.; Dubus, R.; Hofzumahaus, A.; Holland, F.; Wahner, A.; Fuchs, H. Temperature-dependent rate coefficients for the reactions of OH radicals with selected alkanes, aromatic compounds, and monoterpenes *Atmos. Chem. Phys.* **2024**, *24*, 13715–13731.
82. Sage, A. M.; Donahue, N. M. Deconstructing Experimental Rate Constant Measurements: Obtaining Intrinsic Reaction Parameters, Kinetic Isotope Effects, and Tunneling Coefficients from Kinetic Data for OH + Methane, Ethane and Cyclohexane. *J. Photochem. Photobiol. A: Chem.* **2005**, *176*, 238–249.
83. Hu, W.-P.; Truhlar, D. G. Factors Affecting Competitive Ion–Molecule Reactions: ClO^- + C_2H_5Cl and C_2D_5Cl via E2 and S_N2 Channels *J. Am. Chem. Soc.* **1996**, *118*, 860– 869.
84. Wu, Y.-R.; Hu, W.-P. Reaction Dynamics Study on the Tunneling Effects of a Microsolvated E2 Reaction: $FO^-(H_2O) + C_2H_5Cl \rightarrow HOF(H_2O) + C_2H_4 + Cl^-$ *J. Am. Chem. Soc.* **1999**, *121*, 10168-10177.
85. Tsai, W.-C.; Hu, W.-P. Theoretical Analysis on the Kinetic Isotope Effects of Bimolecular Nucleophilic Substitution (S_N2) Reactions and Their Temperature Dependence. *Molecules* **2013**, *18*, 4816-4843.
86. Kang, B.; Radosavich, A. T. ^{18}O Kinetic Isotope Effect Evidence for a Concerted [3 + 1] Cycloaddition in Phosphetane-Catalyzed Reductive N-Arylation of Nitroarenes. *Tetrahedron* **2025**, *186*, 134892.
87. Karmakar, S.; Datta, A. Heavy-Atom Tunneling in Organic Transformations. *J. Chem. Sci.* **2020**, *132*, 127.
88. Zuev, P. S.; Sheridan, R. S.; Albu, T. V.; Truhlar, D. G.; Hrovat, D. A.; Borden, W. T. Carbon Tunneling from a Single Quantum State. *Science* **2003**, *299*, 867.
89. Gonzalez-James, O. M.; Zhang, X.; Datta, A.; Hrovat, D. A.; Borden, W. T.; Singleton, D. A. Experimental Evidence for Heavy-Atom Tunneling in the Ring-Opening of Cyclopropylcarbinyl Radical from Intramolecular $^{12}C/^{13}C$ Kinetic Isotope Effects. *J. Am. Chem. Soc.* **2010**, *132*, 12548.
90. Chen, J. -L.; Hu, W. -P. *Theoretical Prediction on the Thermal Stability of Cyclic Ozone and Strong Oxygen Tunneling.* J. Am. Chem. Soc. **2011**, 133, 16045-16053.